



ELSEVIER

Magnetic Resonance Imaging 20 (2002) 413–424

MAGNETIC  
RESONANCE  
IMAGING

# Numerical calculations of the static magnetic field in three-dimensional multi-tissue models of the human head

Christopher M. Collins<sup>a,\*</sup>, Bei Yang<sup>a</sup>, Qing X. Yang<sup>a</sup>, Michael B. Smith<sup>a,b</sup>

<sup>a</sup>Department of Radiology, The Pennsylvania State University College of Medicine, 500 University Drive, Hershey, PA 17033, USA

<sup>b</sup>Department of Cellular and Molecular Physiology, The Pennsylvania State University College of Medicine, 500 University Drive, Hershey, PA 17033, USA

Received 2 February 2002; accepted 5 May 2002

## Abstract

Susceptibility-induced perturbation of the static magnetic field by the human body during magnetic resonance imaging (MRI) leads to undesirable artifacts as well as valuable physiological information, as in functional MRI. The ability to calculate these perturbations for a multi-tissue human body model provides a powerful tool in designing hardware and acquisition methods for reducing the artifacts, and in relating observed image contrast to physiological origins. We have developed a method for calculating the static field in arbitrary 3D magnetic susceptibility distributions and performed calculations in a complete model of the human head and shoulders. The accuracy of our method was validated in regular geometries with known analytical solutions and in comparison with experimental results acquired from the head of the same human subject used for computer modeling. Results are presented in parts per million (ppm) deviation from the applied field strength and are valid for any imaging or spectroscopy system. © 2002 Elsevier Science Inc. All rights reserved.

*Keywords:* Calculation;  $B_0$ ; MRI; Magnetic susceptibility; Inhomogeneity

## 1. Introduction

Differences in relative magnetic permeability ( $\mu_r$ ) between various tissues provide a physical mechanism for the detection of important pathology and physiology using MRI techniques such as functional MRI (fMRI) [1]. Unfortunately, the differences in  $\mu_r$  between tissues and air can generate strong static magnetic field ( $B_0$ ) inhomogeneity, resulting in severe loss of signal and image distortion artifacts [2,3]. The useful image contrast that is used to detect the subtle changes in  $B_0$  is adversely affected by strong  $B_0$  inhomogeneity near air-tissue interfaces because the susceptibility contrast and artifacts have the same physical origin. Some of the most prominent examples of  $\mu_r$ -related signal loss near air-containing structures in the human body are seen in the regions of the brain above the nasal cavity and sphenoid sinus [2]. A detailed knowledge of the  $B_0$  field distribution in the human body is necessary for a better understanding of image distortion so that more effective correction techniques can be devised. The ability to accu-

rately model the  $B_0$  field in the human body will also allow for investigations of the many important physiological and pathologic changes associated with susceptibility changes. Thus, a thorough understanding of the interactions between the  $B_0$  field and the human body is fundamentally important for scientific utilization of MRI.

Theoretical analysis of such interactions is extremely difficult because of the irregular geometry and complicated  $\mu_r$  distribution of the human body. In the past, the  $B_0$  field has been calculated in several simple structures [2–8], including a single-tissue three-dimensional human head model [2] and single-tissue, two-dimensional head models [6,7]. The success of these models at predicting the field distortions seen in MRI were necessarily limited by their simplification, and because all tissues were treated as water it was not possible to calculate the subtle distortions caused by intra-tissue permeability differences. The models developed in this work take into account many more tissues than the previous models, including the permeability values of air, water, bone, gray matter, white matter, fat and blood.

A finite-difference static magnetic field solver was developed and shown to have an average error of a few parts per billion for cases with known analytical solutions. The solver's accuracy is a function of both spatial resolution of

\* Corresponding author. Tel.: +1-717-531-6069; fax: +1-717-531-8486.

E-mail address: cmcollins@psu.edu (C. Collins).

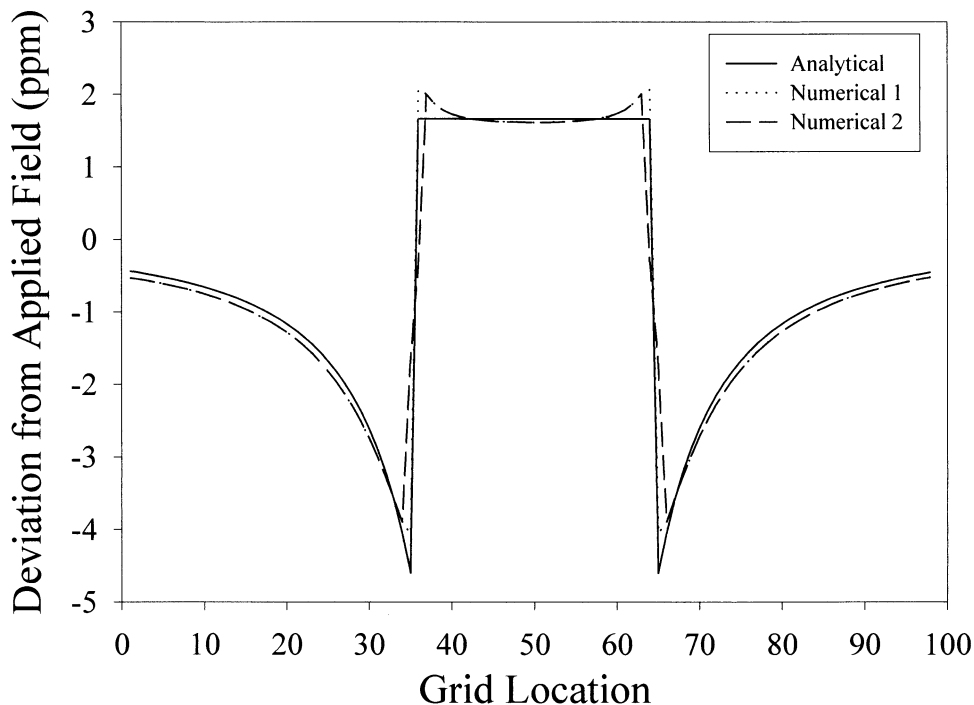


Fig. 1.  $B_0$  field magnitudes in sphere of water immersed in air using an analytical solution (Analytical, solid) forward- and backward-difference approximations at interfaces between dissimilar materials as described in the text (Numerical 1, dotted line) and central-difference approximations everywhere (Numerical 2, dashes).

the model and the convergence criteria used during the calculation process. Using this static magnetic field solver, the static magnetic distribution in multi-tissue models of the human head were calculated and compared with experimental measurements.

## 2. Methods

### 2.1. Creation of static magnetic field solver

An initially homogeneous  $B_0$  field is perturbed when an object having a distribution of  $\mu_r$  values not equal to that of

the background medium (air, in most cases) is introduced. The perturbed magnetic field distribution can be obtained by first solving

$$\nabla \cdot (\mu_r \nabla \Phi) = 0 \quad (1)$$

where  $\Phi$  is the magnetic scalar potential. Once the magnetic scalar potential is obtained, the magnetic flux density can be calculated as

$$\mathbf{B} = \mu_0 \mu_r (-\nabla \Phi) \quad (2)$$

where  $\mu_0$  is the magnetic permeability of free space. In MRI, the field that is experienced by the nuclei is the

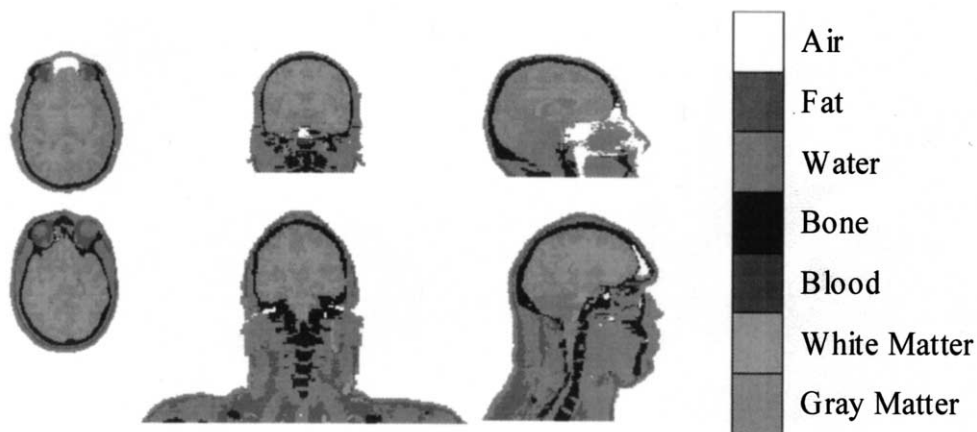


Fig. 2. Distributions of  $\mu_r$  in the MRI-based model (top) and the NLM-based model (bottom) in three orthogonal planes.

microscopic field,  $\mathbf{B}_0$ . The  $\mathbf{B}_0$  field can be obtained from  $\Phi$  by considering the Sphere of Lorentz as in Eq. (3) [4,9].

$$\mathbf{B}_0 = \mu_0 \mu_r \left( 1 - \frac{2}{3} (\mu_r - 1) \right) (-\nabla \Phi) \quad (3)$$

Here the nucleus is assumed to be within a small sphere of free space. This approach is theoretically sound and has been proven accurate with experiment [9].

A computer program was developed in C++ to iteratively calculate the distribution of  $\Phi$  for a given  $\mu_r$  distribution and an initial guess of  $\Phi$ . Three-dimensional double precision floating-point arrays were used to represent the three-dimensional distributions of  $\mu_r$ ,  $\Phi$ , and  $\mathbf{B}_0$ .

To solve Eq. (1) using finite difference (FD) approximations, an iterative coordinate,  $T$  (pseudo-time), is introduced and Eq. (1) is rewritten as

$$\frac{\partial \Phi}{\partial T} = \nabla \cdot (\mu_r \nabla \Phi). \quad (4)$$

As the solution converges toward the correct answer, both sides of Eq. [4] will approach 0 [see Eq. (1)]. To solve for  $\Phi$  using the FD method, a four-dimensional grid in space and pseudo-time with spatial resolutions of  $\Delta x$ ,  $\Delta y$ , and  $\Delta z$ , and a pseudo-temporal resolution of  $\Delta T$  was introduced with indices of  $i$ ,  $j$ ,  $k$ , and  $t$  assigned to identify locations in the  $x$ ,  $y$ ,  $z$ , and  $T$  directions respectively. In this coordinate system, Eq. (4) was rewritten as

$$\Phi(t) = \Phi(t-1) + \Delta T (\Phi_x + \Phi_y + \Phi_z) \quad (5)$$

where

$$\Phi_x = \frac{\partial \mu_r}{\partial x} \frac{\partial \Phi(t-1)}{\partial x} + \mu_r \frac{\partial^2 \Phi(t-1)}{\partial x^2} \quad (6)$$

$$\Phi_y = \frac{\partial \mu_r}{\partial y} \frac{\partial \Phi(t-1)}{\partial y} + \mu_r \frac{\partial^2 \Phi(t-1)}{\partial y^2} \quad (7)$$

$$\Phi_z = \frac{\partial \mu_r}{\partial z} \frac{\partial \Phi(t-1)}{\partial z} + \mu_r \frac{\partial^2 \Phi(t-1)}{\partial z^2} \quad (8)$$

To ensure that  $\Phi$  will converge toward the correct solution, it is important to ensure that  $\Delta T$  is sufficiently small [4]. After an initial guess for  $\Phi(t=0)$  is created, values for  $\Phi$  at each consecutive point in pseudo-time are calculated at every interior location in the problem space using Eqs. (5–8) with first order central difference approximations for all partial derivatives with respect to space. Values for  $\Phi$  are calculated at consecutive, future points in pseudo-time until a specified convergence criterion is reached.

To reduce the computational requirements by minimizing the size of the problem without compromising the spatial resolution, the problem region contains only the sample and its immediate surrounding volume (with a minimum 10-cell distance between the model and the boundary). The magnetic field at the boundary of this region is significantly altered by the sample and is thus not known initially. To efficiently calculate the field distribution at the boundary,

we first performed a preliminary calculation: a full field calculation for a preliminary lower-resolution (three times the grid dimensions) version of the model with a much larger problem region (three times the problem region dimensions). This method is similar to the one implemented by Bhagwandien et al. [4] but with only one preliminary calculation. In the preliminary calculation, the boundary is remote from the perturbing object. The magnetic field at the boundary can be considered uniform and  $\Phi(t=0)$  is determined accordingly. The preliminary calculation is started with an initial guess for  $\Phi(t=0)$  assuming a uniform magnetic field. In this case,  $\Phi(t=0)$  is defined as a function of location that has a constant, non-zero first derivative in the direction of the initially applied homogeneous magnetic field. Then  $\Phi$  is calculated for this preliminary calculation iteratively using Eqs. (5–8) until a specified convergence criterion is reached. Subsequently, the  $\Phi(t=0)$  distribution for the desired problem region and resolution is obtained by interpolating values from the preliminary solution.

To assure convergence for all points, a parameter  $\epsilon$  to follow convergence was defined as

$$\epsilon \equiv \frac{\sum |\Phi(t) - \Phi(t-1)|}{N} \quad (9)$$

where the summation was performed over every grid point in the problem region and  $N$  is the total number of grid points in the problem region. The criterion for convergence was defined as when  $\epsilon$  reached a value ranging from  $7 \times 10^{-6}$  for the National Library of Medicine (NLM)-based head model (described later in this work) to zero (fully converged to the extent of the precision of a double precision floating point variable) for all other calculations. Calculations were performed on an 800 MHz Pentium III PC having 512 MB RAM. An  $\epsilon$  of  $7 \times 10^{-6}$  for the NLM-based model can be shown to correspond to an average per-iteration change in  $\mathbf{B}_0$  values of about 4.4 parts per billion. Calculation time ranged from 4 min for a low-resolution cylinder to approximately 150 h for the NLM-based head model.

After  $\Phi$  is found to an acceptable precision at the desired resolution, the  $\mathbf{B}_0$  field is calculated using Eq. (3) and first-order FD approximations. Rather than using central

Table 1  
Relative magnetic permeability ( $\mu_r$ ) values assigned to different tissues.

Material	$\mu_r$	Reference
Free Space	1.00000000	—
Air	1.00000040	10
Water	0.99999096	11
Fat	0.99999221	11
Bone	0.99999156	11
Blood	0.99999153	12
Gray Matter	0.99999103	—
White Matter	0.99999120	—

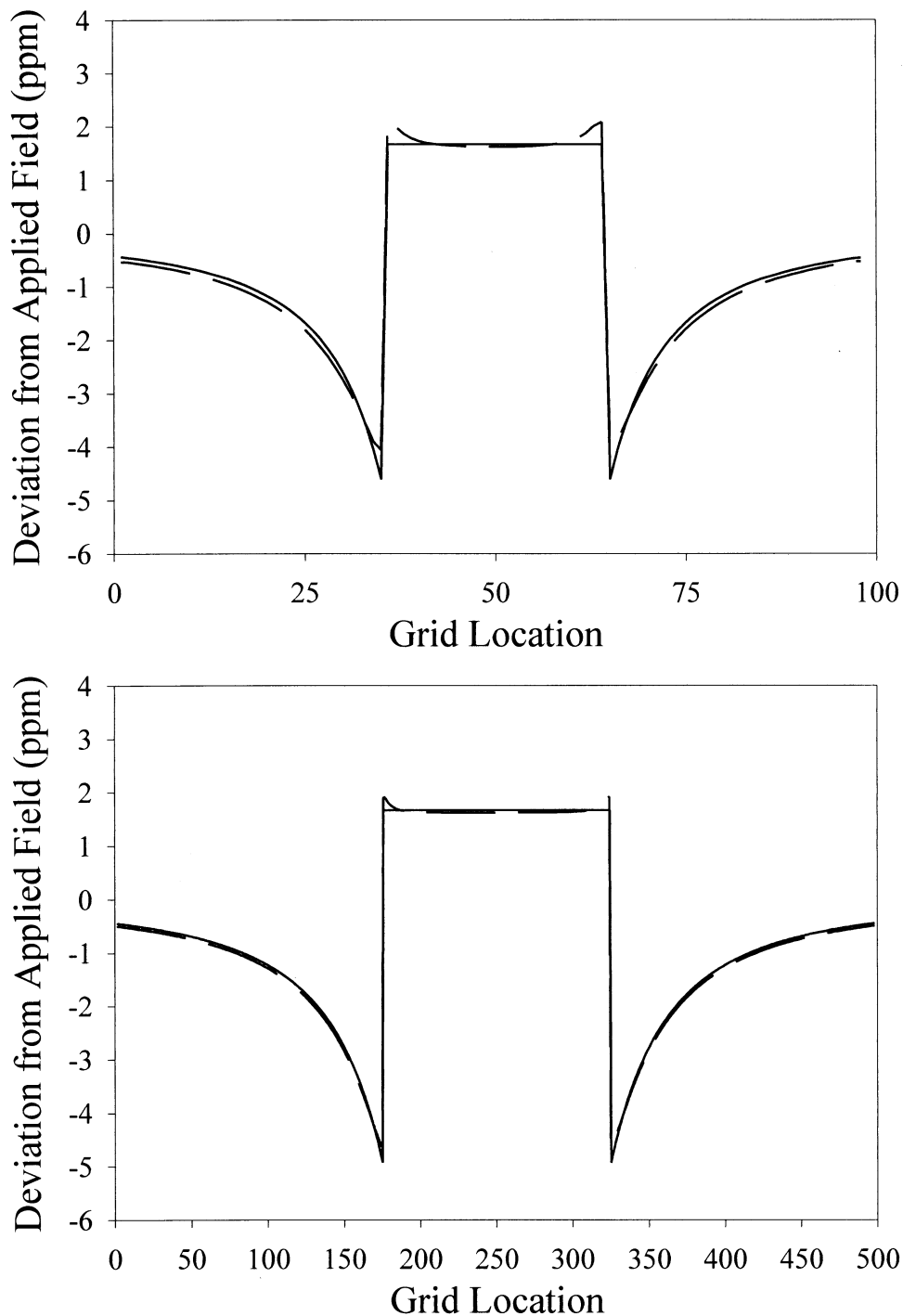


Fig. 3. Analytically (solid) and numerically (dashed) calculated  $\mathbf{B}_0$  field magnitude distribution along a line oriented with the applied  $\mathbf{B}_0$  field and passing through the center of a low-resolution (top) and high-resolution (bottom) cylinder of water immersed in air. Ordinate scale is in parts per million deviation from applied field.

difference approximations at all locations in finding  $\nabla\Phi$ , however, forward and backward difference approximations were used so that only values within one material were used in the approximations. This was seen to reduce error near the interface between materials with different  $\mu_r$ . Fig. 1 shows a comparison between the analytical and numerical

$\mathbf{B}_0$  field magnitudes in a sphere using central difference approximations everywhere in finding  $\nabla\Phi$ , and using forward and backward differences at the interfaces between dissimilar materials. The calculated values match the analytical solution more closely when the forward and backward difference approximations are used.

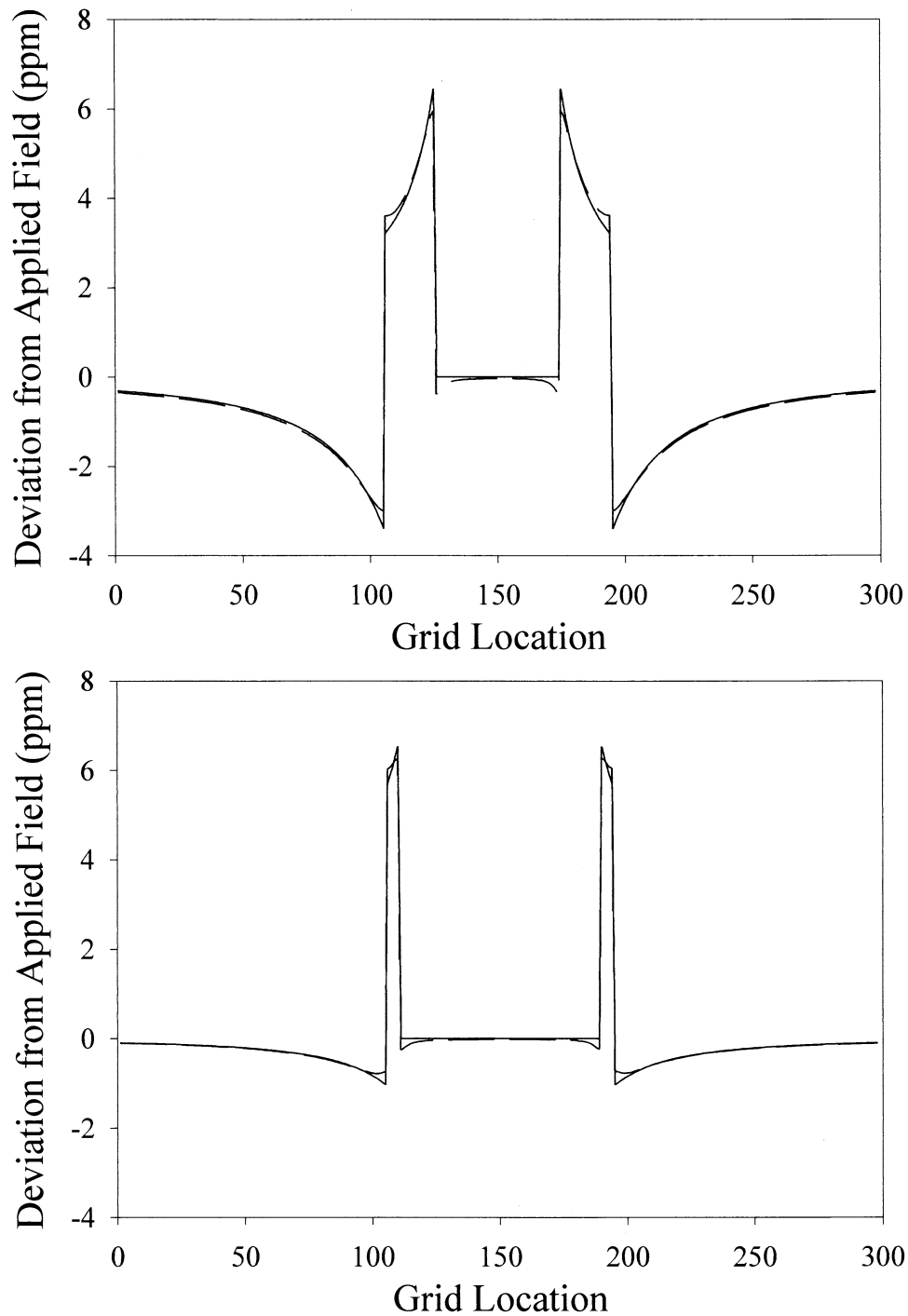


Fig. 4. Analytically (solid) and numerically (dashed) calculated  $B_0$  field magnitude distribution along a line oriented with the applied field and passing through the center of a thick (top) and thin (bottom) cylindrical shell of water immersed in free space.

## 2.2. Creation of the head models

Two 3D multi-tissue models of the human head were created for use with the static magnetic field solver. The first (MRI-based) model was created from a 3D MRI data set acquired from a human subject. The experimental  $B_0$  field maps were also acquired from this subject in the same

position in the magnet after the 3D image data were collected so that a comparison with the numerical result could be carried out. The method for acquisition of the experimental field maps has been described previously [2]. The second (NLM-based) model was created from the digital photographic images of a cadaver from the National Library of Medicine's Visible Male project.

The images for both models were segmented and assembled into a 3D model in the same fashion. Using Adobe Photoshop 3.0, the 2D images of cross sectional slices were segmented into different tissues and assigned unique colors in RGB (red, green, blue: intensity values range from 0 to 255) format. After the images had been segmented, the images' different RGB values were assigned integer values used as ID numbers for specific tissues and assembled into a three dimensional array via a program written in Interactive Data Language (IDL). After the three dimensional array was assembled,  $\mu_r$  values replaced the ID numbers and the final model was made. The  $\mu_r$  values of air, water, bone, fat, and deoxygenated blood were obtained from various sources [10–12], while the  $\mu_r$  values of gray matter and white matter were estimated using weighted averages of fat and water content. The  $\mu_r$  values used for the different tissues are presented in Table 1. All tissues that are not on Table 1 were treated as water.

The MRI-based model, extending from the top of the head to just below the lower lip, had a problem region of 25.6 cm (128 cells) with a spatial resolution of 2 mm/cell in each direction. The NLM-based model, extending from the top of the head to top of the lungs, had a problem region of

62 cm (309 cells), 35.6 cm (175 cells), and 39.75 cm (159 cells) in the left-right, anterior-posterior, and inferior-superior directions respectively. The resolution of the NLM-based model was 2 mm/cell in the left-right and anterior-posterior directions, and 2.5 mm per cell in the inferior-superior direction. The permeability distributions on three orthogonal planes through the two models are shown in Fig. 2.

### 2.3. Validation

The accuracy of the static magnetic field solver was validated rigorously by careful comparisons of the numerical solutions with the analytical solutions of simple geometries immersed in air or in free space. These geometries include low- and high-resolution cylinders of water, thin and thick cylindrical shells of water, and a sphere of water. For further validation, the static magnetic field inside a human head (MRI-based model) was calculated and compared with experimentally measured results.

The models of the cylinders that were used for calculation consisted of a low-resolution and a high-resolution cylinder. The high-resolution cylinder had a problem region of  $500 \times 500$  cells and a radius of 75 cells while the

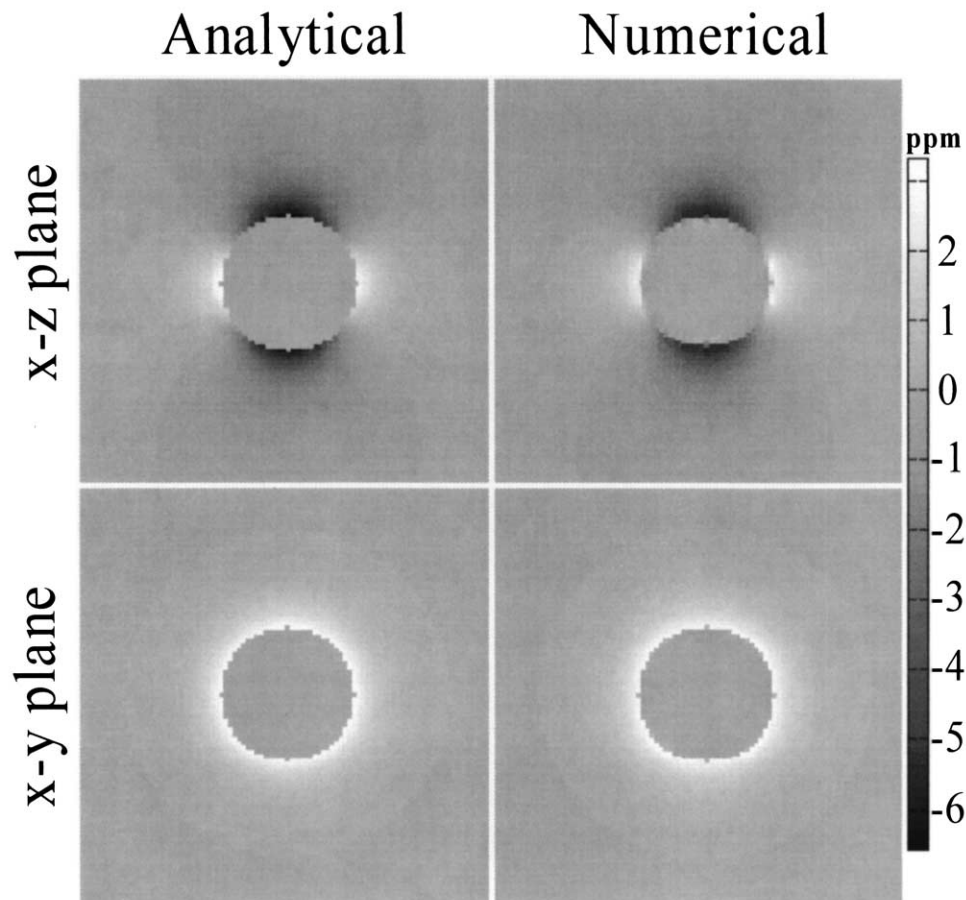


Fig. 5. Grayscale plots of the analytically (left) and numerically (right) calculated  $\mathbf{B}_0$  field magnitude in a sphere of water immersed in free space. Scale is in parts per million deviation from the applied field. The applied field is oriented in the z direction.

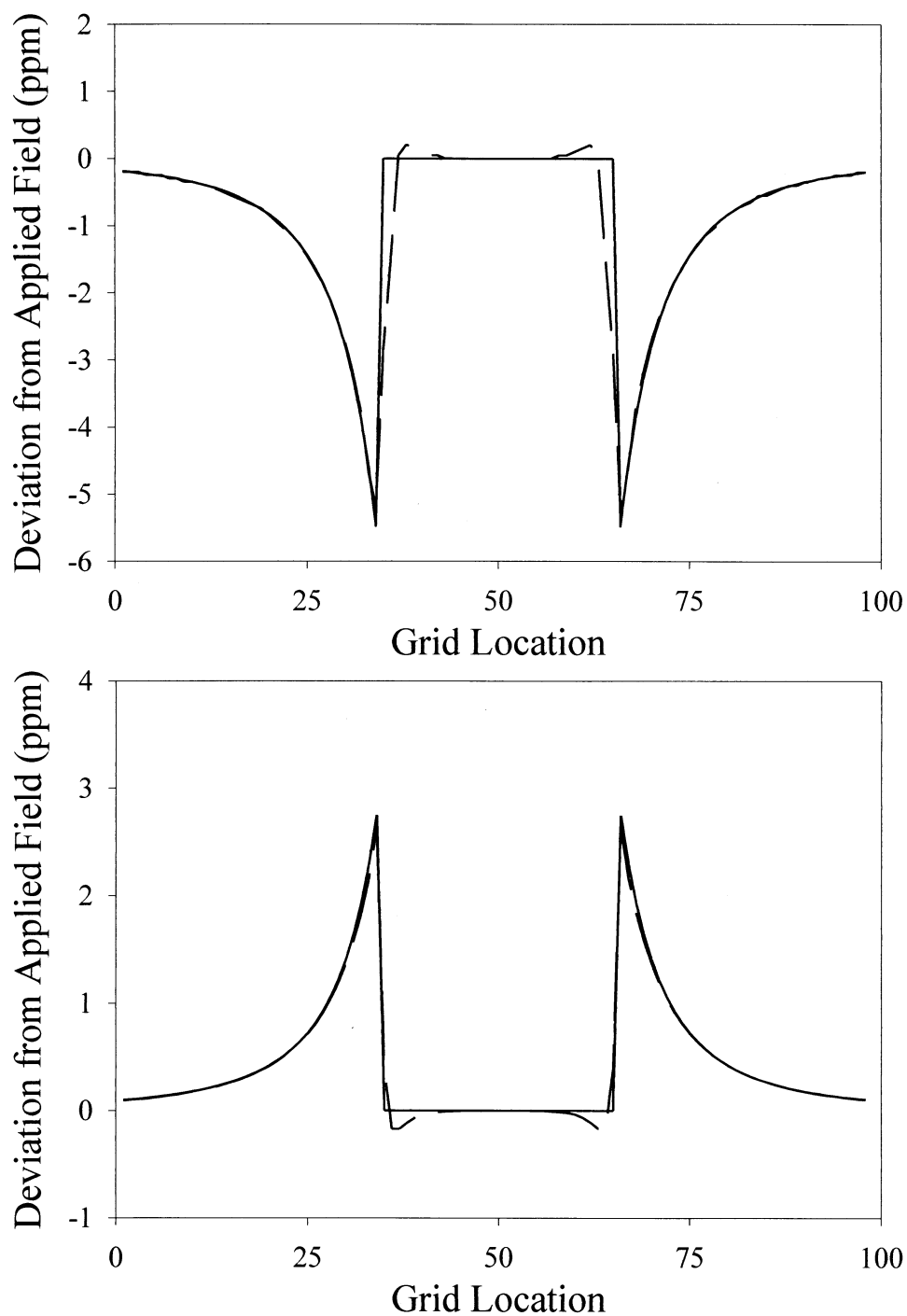


Fig. 6. Analytically (solid) and numerically (dashed) calculated  $B_0$  field magnitude distribution along lines oriented in parallel (top) and perpendicular (bottom) to the applied field and passing through the center of a low-resolution sphere of water immersed in free space.

low-resolution cylinder had a problem region of  $100 \times 100$  cells and a radius of 15 cells. The models of the cylindrical shells used for calculation consisted of a thin and a thick shell. The two shells both had a problem region of  $300 \times 300$  cells. While the outer radius was identical (45 cells) in each solution, the inner radius was 25 cells for the thick shell and 40 for the thin shell. Thus, the thin shell had a thickness of 5 cells and the thick shell had a thickness of 20 cells. The

model of the sphere had a problem region of 100 cells in each dimension and radius of 15 cells.

### 3. Results

Line plots of the calculated and analytical  $B_0$  field magnitude distribution through a low-resolution and high-reso-

Table 2  
Absolute deviation between analytical and numerical calculation results (error) for low-resolution sphere.

	Maximum	Minimum	Average
Absolute deviation (ppm)	2.85	$2 \times 10^{-9}$	$3.84 \times 10^{-3}$

lution cylinder of water in free space are shown in Fig. 3. In these plots, the line passes through the center of the cylinder and is oriented in the same direction as that of the applied field. The scale of the ordinate is in parts per million (ppm) deviation from the applied field. The agreement between analytical and numerical calculations is excellent. The largest difference between analytically- and numerically calculated values (less than 0.2 ppm) occurs about the interface between the cylinder and air. In the higher-resolution cylinder, this region of higher error is reduced (relative to the cylinder radius).

To assess the solver's ability to handle the models with multiple layers of distinct materials, the analytically- and numerically calculated  $\mathbf{B}_0$  field distributions of a cylindrical shell of water in free space are compared. Line plots of the analytically- and numerically calculated  $\mathbf{B}_0$  field magnitude distribution through the thin and thick cylindrical shells are shown in Fig. 4. As in Fig. 3, the line passes through the center of the inner cylinder and is oriented in the same direction as that of the applied field. The agreement between analytical and numerical calculations is excellent everywhere, with the only noticeable differences near the interface between the cylinder and free space. The use of the thin shell appears to induce no greater error than does the thick shell. Thus, the static magnetic solver can produce accurate  $\mathbf{B}_0$  solutions for models with subtle features only a few cells thick.

Grayscale cross-sectional plots of the numerical and analytical  $\mathbf{B}_0$  field magnitude distributions in two orthogonal planes passing through the center of a sphere in free space are displayed in Fig. 5. The grayscale is given in parts per million (ppm) deviation from the applied field value. The

applied field is oriented in the z-direction. To better compare the analytical solution with the numerical results, line plots of the analytical and numerical  $\mathbf{B}_0$  field magnitude distributions along lines oriented in two orthogonal directions are shown in Fig. 6. For further analysis of error throughout the problem region, the maximum, minimum, and average absolute difference between analytical and numerical solutions are listed in Table 2. The average difference between the calculated and analytical solution is less than 3 parts per billion, indicating the overall accuracy of the calculated result. The disparity between the maximum (2.85 ppm) and the average differences suggests that there are a few concentrated regions of high errors in the calculated solution. These regions are located near cells having 4–5 of their 6 faces exposed to materials of different  $\mu_r$ . The localized large error due to the limited model resolution is a common problem for numerical methods, related to the limited ability to model smooth curved surfaces using a rectilinear grid. The extent of this problem can be reduced by increasing the model resolution, as shown in Fig. 3.

The  $\mathbf{B}_0$  field magnitude distributions of both the MRI-based and the NLM-based head models were calculated assuming the applied field to be oriented in the superior-inferior (head-foot) direction, as it is in most superconducting human MRI systems. The calculated  $\mathbf{B}_0$  distribution from the MRI-based model is compared with the experimentally measured result of the same subject from whom the model is created. The calculated and measured field deviations on a slice approximately 4 cm above the base of the nose are displayed in Fig. 6. The magnitudes of  $\mathbf{B}_0$  along the two perpendicular lines shown in Fig. 6 are plotted in Fig. 7. The numerical solution is plotted as a solid line while +’s mark the experimentally measured  $\mathbf{B}_0$  field. Both the grayscale plots and the line plots show that the experimental and numerical  $\mathbf{B}_0$  field distributions are in good agreement. Since the MRI-based model only extended to the chin, significant error is expected in the calculated result near the

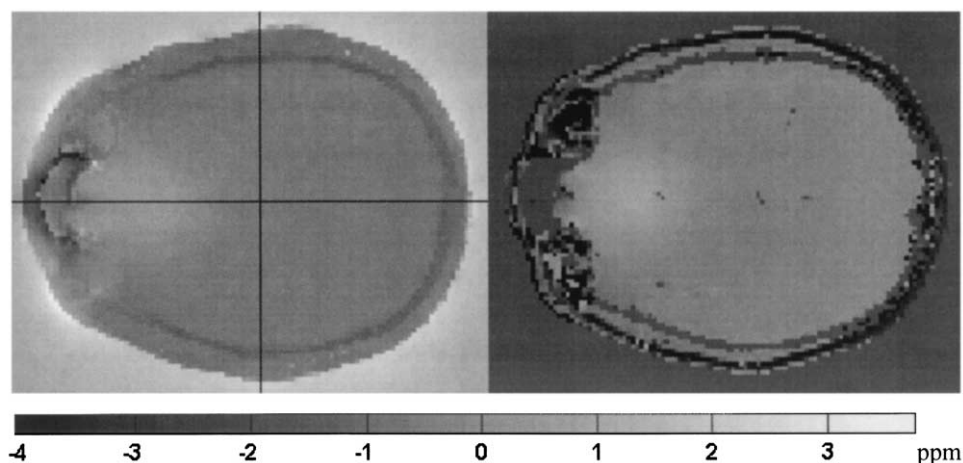


Fig. 7. Numerically calculated (left, MRI-based model) and experimentally measured (right)  $\mathbf{B}_0$  field magnitudes in ppm deviation from the value at intersection of two lines shown. The regions from which experimental data could not be acquired appear black in the experimental plot.

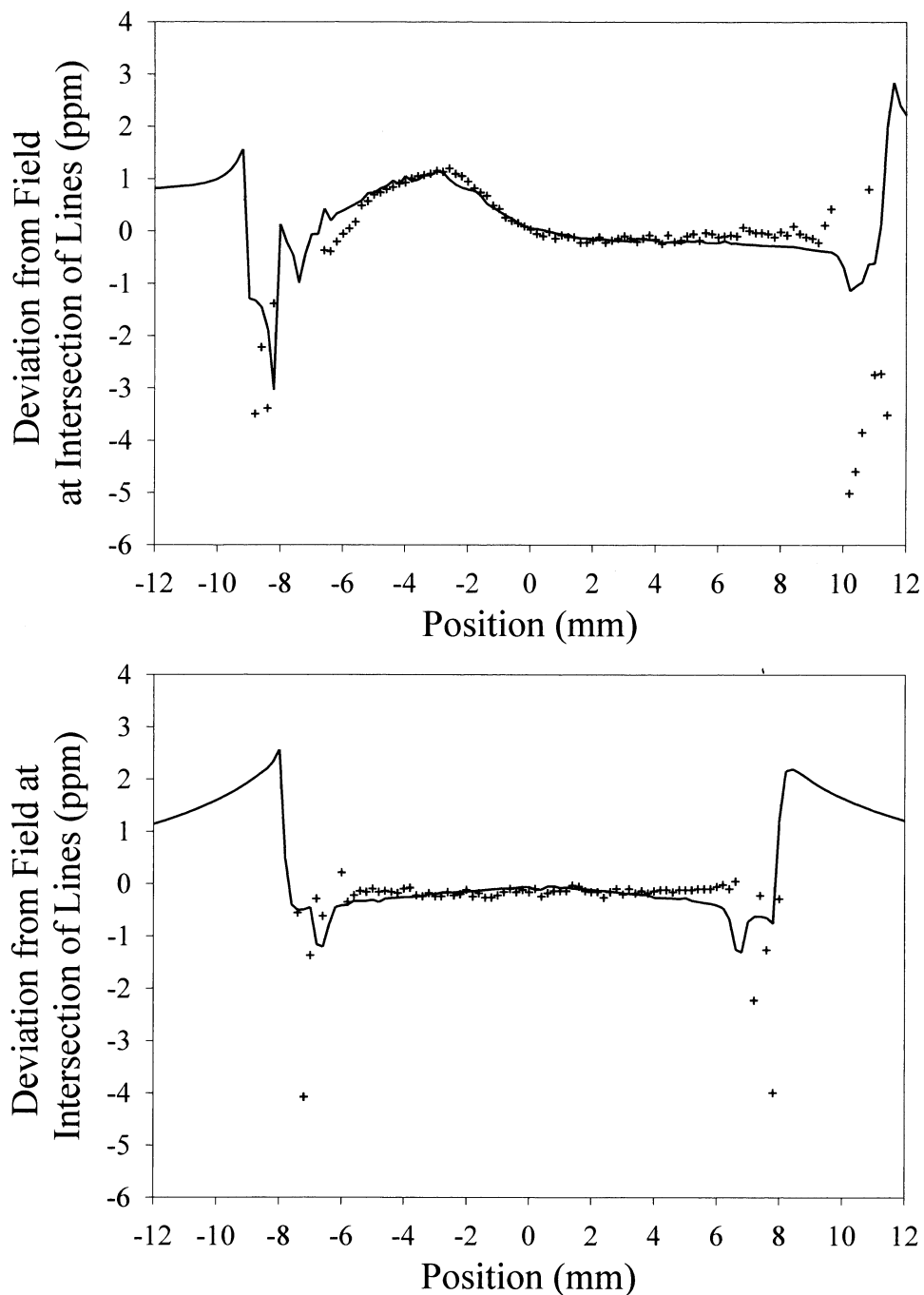


Fig. 8. Experimentally measured (+) and numerically calculated (solid line, MRI-based model)  $B_0$  field magnitudes in ppm deviation along the anterior-posterior (top) and left-right (bottom) lines shown in Fig. 7.

inferior boundary of the model. Thus, an axial slice that was far from the model's inferior boundary was chosen for comparison.

The calculated results with the NLM-based head model provide an accurate  $B_0$  field distribution of an entire brain. The  $B_0$  field magnitudes are displayed by contour lines superimposed on grayscale plots for three sagittal and three coronal planes in Fig. 8, and three axial planes in Fig. 9. Field deviations ranged from 5.6 ppm to  $-6.8$  ppm throughout the head model. All sagittal and coronal grayscale plots are displayed with a range from  $-6$  ppm

to 4.2 ppm and axial plots are displayed on a range from  $-2$  ppm to 1.5 ppm. Contour lines are drawn at values of  $-2$ ,  $-1$ ,  $0$ ,  $1$ , and  $2$  ppm for all figures.

#### 4. Discussion

From comparison of numerical calculations to analytical solutions in simple shapes (Figs. 3–6, Table 2), it is clear

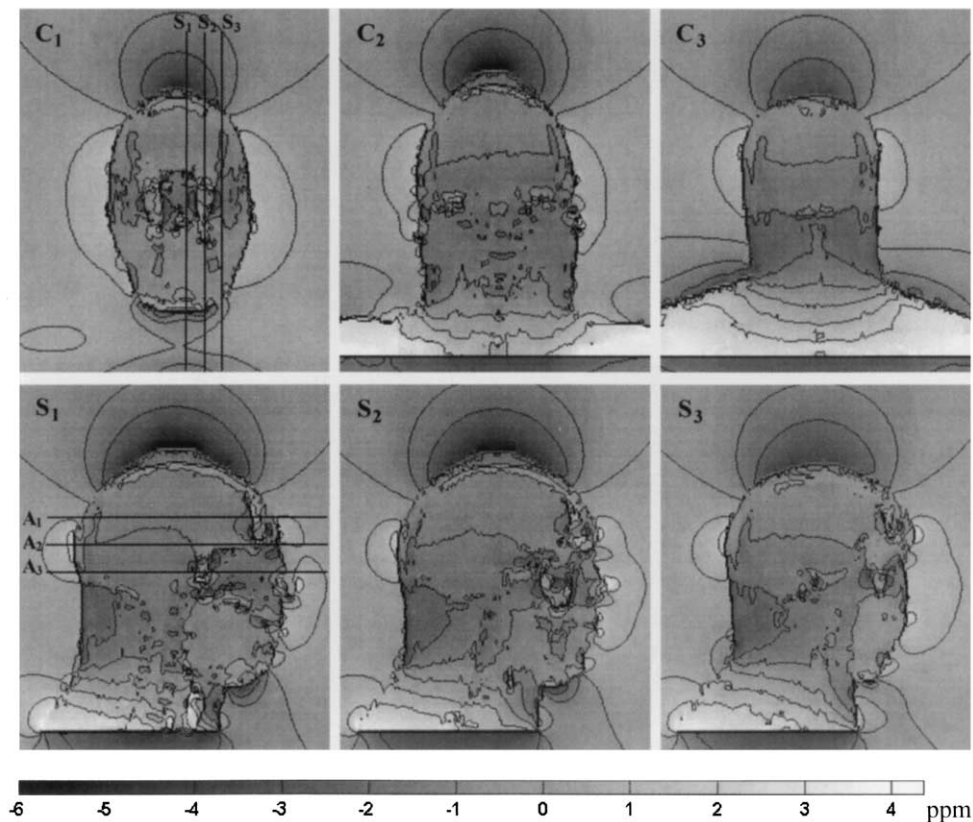


Fig. 9. Numerically calculated  $\mathbf{B}_0$  field magnitudes in ppm deviation from applied field on sagittal (bottom) and coronal (top) planes through the NLM-based head model. Contour lines have been drawn at  $-2$ ,  $-1$ ,  $0$ ,  $1$ , and  $2$  ppm.

that the numerical method developed is capable of calculating the  $\mathbf{B}_0$  field to a great degree of accuracy. The only possible exception to this is at the interface between materials with different  $\mu_r$  values. In these areas the error is still generally less than  $0.5$  ppm.

From comparison of numerical calculations to experimentally measured data in the human head of the same subject (Figs. 7–8), it is evident that utilizing the numerical

method and anatomically accurate models the  $\mathbf{B}_0$  field can be reliably calculated to a great degree of accuracy. The agreement between numerical solution and experiment is excellent within the brain, but there are noticeable differences in the peripheral tissues of the head (skull, subcutaneous fat, skin). In the worst case these differences have magnitudes of about  $3$  ppm. These differences could be due to either limited precision in the numerical calculation or in

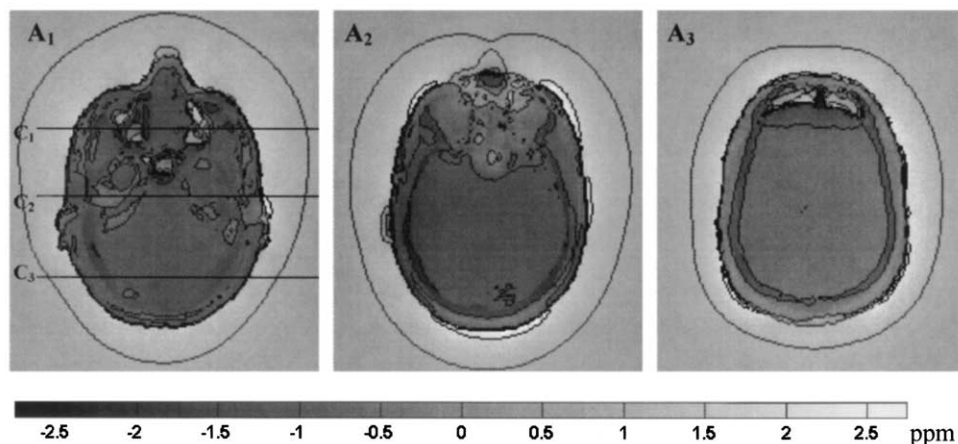


Fig. 10. Numerically calculated  $\mathbf{B}_0$  field magnitudes in ppm deviation from applied field on three different axial planes, spaced  $6.25$  cm apart, through the NLM-based head model. Contour lines have been drawn at  $-2$ ,  $-1$ ,  $0$ ,  $1$ , and  $2$  ppm.

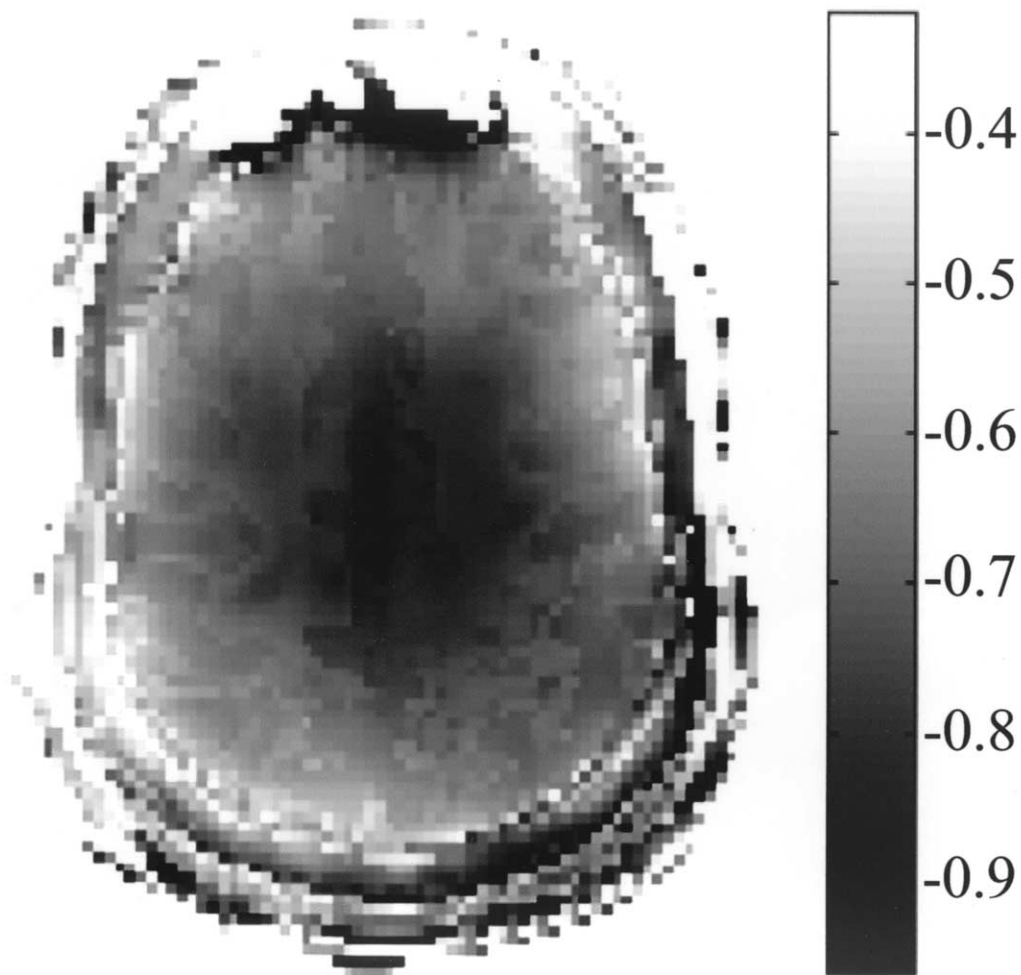


Fig. 11. Numerically calculated  $\mathbf{B}_0$  field magnitudes in ppm deviation from applied field on an axial plane with gray scale set to show difference in  $\mathbf{B}_0$  field due to difference in susceptibility between gray and white matter in the brain.

the experimental measurement. In the experimental measurement there is some volume averaging of tissues with cortical bone and with air in these peripheral regions. One possible source of error in the calculation is in the values for  $\mu_r$  assigned to the tissues in the model. These values are not often measured and can be functions of temperature and other physiological variables. It is possible that some error in this region is due to the existence of several interfaces between dissimilar materials within close proximity to each other. In analytical calculations, however, the proximity of such interfaces (thickness of shell, Fig. 4) did not have a dramatic effect on the accuracy at these interfaces, and there are interfaces between white matter, gray matter, and cerebral-spinal fluid within the brain region of the model that have no significant deviation from the experimental values.

Given the accuracy of  $\mathbf{B}_0$  values calculated with this method inside the human brain where we are interested in the effects of the  $\mathbf{B}_0$  field distribution for MRI experiments, the  $\mathbf{B}_0$  calculated for a complete head model (Figs. 9 and 10)

will provide valuable information to many MRI researchers. As shown in Fig. 9, our calculation predicts a decreasing field gradient visible on the sagittal plane toward the superior-posterior surface of the brain. This feature in the  $\mathbf{B}_0$  distribution can be clearly seen in previous experimental measurements [2], but is absent in previous numerical solutions within a single-tissue 3D model [2]. This indicates that modeling several tissues, including bone, is important for accurate determination of  $\mathbf{B}_0$  field distributions. In addition to the gross field inhomogeneity caused by the air-tissue interfaces in the head, perturbation by the subtle difference in  $\mu$  between different tissue types can be examined with this model. As shown in Fig. 11, the subtle variation in  $\mathbf{B}_0$  between white and gray matter can be seen on an axial slice through the brain by changing the gray scale values. The  $\mu$ -related contrast between white matter and gray matter has been demonstrated experimentally [13]. With this example, we demonstrate that utilization of our numerical method with multi-tissue model provides a po-

tential application in studying the  $\mu$ -related pathologic and physiological changes such as iron deposition in Parkinson's Disease and BOLD effect in fMRI.

The focus of previous experimental and numerical calculation studies has been on the gross  $\mathbf{B}_0$  inhomogeneity by the air-containing structures in the human head. As shown in Table 1, the difference in  $\mu$  between gray mater and white matter is expected to be about two orders of magnitude smaller than that between air and brain tissues. It is experimentally difficult to produce image contrast that is sensitive to detect such subtle variations in  $\mu$  without strong interference from  $\mathbf{B}_0$  inhomogeneity artifacts. While in this work we are primarily interested in introducing and verifying our calculation method and thus have not yet examined subtle changes in  $\mu$  distribution important for techniques as sensitive as fMRI, with this calculation method a number of important studies could be performed. For example, the influence of gross  $\mathbf{B}_0$  inhomogeneity could be removed by changing the susceptibility of air in the head to reveal the tissue specific contrast. Effects of respiration [8] and other sources of physiological noise can be added to the model. Effects of local contrast due to susceptibility and blood volume changes in the head can be examined. All of these things will allow us to differentiate and classify the contributions from the different sources and aid in attempts to identify the contrast mechanisms associated with certain physiological processes.

## 5. Conclusions

We have developed a method for calculation of the static magnetic field in arbitrary shapes containing multiple magnetic susceptibilities and demonstrated its accuracy by comparison to both analytical calculations and experimental measurement.

The  $\mathbf{B}_0$  field distributions calculated with this method have the potential to provide a wealth of information for the MRI community. This numerical method coupled with the multi-tissue model can be used in future studies examining the physiological basis for  $\mu_r$ -related changes seen during

MRI experiments. The careful work of method development and validation given here, including the first experimental validation of a  $\mathbf{B}_0$  calculation method in an identical human head (Figs. 7 and 8), lay a solid foundation for future studies of susceptibility-induced contrast and artifacts.

## References

- [1] Kennan RP, Scanley BE, Innis RB, Gore JC. Physiological basis for BOLD MR signal changes due to neural stimulation: separation of blood volume and magnetic susceptibility effects. *Magn Reson Med* 1998;40:840–6.
- [2] Li S, Dardzinski BJ, Collins CM, Yang QX, Smith MB. Three-dimensional mapping of the static magnetic field inside the human head. *Magn. Reson. Med* 1996;36:705–14.
- [3] Ludeke KM, Roschmann P, Tischler R. Susceptibility artefacts in NMR imaging. *Magn Reson Imag* 1985;3:329–43.
- [4] Bhagwandien R, Moerland MA, Bakker CJG, Beersma R, Lagendijk JJW. Numerical analysis of the magnetic field for arbitrary magnetic susceptibility distributions in 3D. *Magn Reson Imag* 1994;12:101–7.
- [5] Bhagwandien R, van Ee R, Beersma R, Bakker CJ, Moerland MA, Lagendijk JJ. Numerical analysis of the magnetic field for arbitrary magnetic susceptibility distributions in 2D. *Magn Reson Imag* 1992;10(2):299–313.
- [6] Bhagwandien R. Object induced geometry and intensity distortions in magnetic resonance imaging. Doctoral Dissertation, University of Utrecht, 1994.
- [7] Li S, Williams GD, Frisk TA, Arnold BW, Smith MB. A computer simulation of the static magnetic field distribution in the human head. *Magn Reson Med* 1995;34:268–75.
- [8] Chu SCK, Xu Y, Balschi JA, Springer CS. Bulk magnetic susceptibility shifts in NMR studied of compartmentalized samples: use of paramagnetic reagents. *Magn Reson Med* 1991;11:2–6.
- [9] Raj D, Paley DP, Anderson AW, Kennan RP, Gore JC. A model for susceptibility artefacts from respiration in functional echo-planar magnetic resonance imaging. *Phys Med Biol* 2000;45:3809–20.
- [10] Krauss JD. *Electromagnetics*. New York: McGraw-Hill, 1984, p. 216.
- [11] Hopkins JA, Wehrli FW. Magnetic susceptibility measurement of insoluble solids by NMR: magnetic susceptibility of bone. *Magn Reson Med* 1997;37:494–500.
- [12] Weisskoff RM, Kiihne S. MRI susceptometry: image-based measurement of absolute susceptibility of MR contrast agents, and human blood. *Magn Reson Med* 1992;24:375–83.
- [13] Reichenbach JR, Venkatesan R, Yablonsky DA, Thompson MR, Lai S, Haacke EM. Theory and application of static field inhomogeneity effects in gradient-echo imaging. *J Magn Reson Imag* 1997;7:266–79.